J. Fluid Mech. (1996), *vol.* 322, *pp.* 81–107

Mixing driven by vertically variable forcing: an application to the case of Langmuir circulation

By ANAND GNANADESIKAN†
Department of Physical Oceanography, Woods Hole Oceanographic Institution, MA 02543, USA

(Received 30 January 1995 and in revised form 14 March 1996)

Two-dimensional mixing driven by an instability mechanism which is concentrated near one of the boundaries is considered, with particular application to Langmuir circulations driven by a wave spectrum. The question of how to define the equivalent of the Rayleigh number is attacked using the energy balance equations and simple truncated models of the instability. Given a particular horizontal wavelength for the disturbance, the strength of the forcing on the cells, and thus the growth rate, is determined by a tradeoff between maximizing the depth-averaged forcing and maximizing the depth of penetration. As a result of this tradeoff, long-wavelength cells grow more slowly, but penetrate more deeply and have a larger equivalent Rayleigh number. At finite amplitude, these long-wavelength cells come to dominate the flow field. The depth of penetration of, and density transport accomplished by, Langmuir cells is considered as a function of the mean stratification and diffusion. An application to oceanic mixed layers is considered assuming the Mellor–Yamada $2\frac{1}{2}$-level turbulence closure model to define the background level of turbulent mixing. For many realistic cases, Langmuir cells are predicted to dominate the vertical transport of momentum and density.

1. Introduction

Over the past century, much insight into the physics of mixing driven by buoyancy forces (Rayleigh–Bénard convection and double-diffusive convection in particular) has been gained by considering the behaviour of the turbulent field as a function of the bulk Rayleigh number. As the Rayleigh number (essentially giving the ratio of the buoyant to diffusive forces) increases, the turbulence becomes more and more energetic, the vertical fluxes of all quantities increase, and occasionally large-scale flows can develop (Howard & Krishnamurti 1986). The Rayleigh number is easily defined when the initial gradients of all quantities do not vary with depth. However, in many environmental situations such is not the case. The question of how to define the Rayleigh number is taken up for one such case, that of Langmuir circulations driven by wave–current interaction.

Langmuir circulations consist of helical counter-rotating vortices in the upper layer of oceans and lakes which are oriented at some small angle α relative to the wind. The surface convergence zones are associated with enhanced concentrations of bubbles, rows of weed and debris, and jets with velocity in the alongcell direction (see Leibovich 1983 for a review). The cells were first described in a quantitative sense by Langmuir (1938) who theorized that they were the principal mechanism by which the mixed layer in ocean and lakes was maintained.

† Present address: Program in Atmospheric and Oceanic Sciences, Princeton University, PO Box CN710 Princeton, NJ 08540, USA. email: alg@gfdl.gov.

In the 1970s, a series of papers (Craik 1970; Craik & Leibovich 1976; Leibovich 1977*a*: Huang 1979) established a possible forcing mechanism for Langmuir cells involving interactions between surface gravity waves and the mean Eulerian shear. These equations (presented in detail later in this work) treat Langmuir cells as a sort of double-diffusive convection, where the *mean Eulerian velocity* is the destabilizing field and density acts as a stabilizing field. The mechanism works as follows. Horizontal perturbations in the Eulerian velocity are rotated into the plane of the cells by the Stokes drift shear associated with the surface gravity waves (figure 1*a*). The rate at which this tilting occurs is proportional to the Stokes drift shear. The vortices created by this interaction then act on the mean Eulerian shear to reinforce the horizontal perturbations (figure 1*b*) in alongcell velocity. The rate at which this reinforcement occurs is proportional to the Eulerian shear. The growth rates associated with the Craik–Leibovich wave–current interaction mechanism thus go as the *geometric mean* of the Stokes drift shear and Eulerian shear.

In order for observational oceanographers to evaluate whether this mechanism is important for driving Langmuir circulations, it is necessary to evaluate the strength of the wave–current interaction mechanism relative to the high 'background' turbulent mixing found within the mixed layer, i.e. to define the equivalent of a Rayleigh number. This is rendered difficult by two factors. (i) The background viscosity is not well known when mixing is strong and probably varies with depth. Because of the presence of a surface wave stirred layer, however, the mixing coefficient may vary by less than an order of magnitude over shallow mixed layers of less than 40 m (Terray *et al.* 1996). (ii) The Stokes drift and Eulerian shears are even more variable with depth. For one simple wave spectrum (that of Pierson & Moskowitz 1964) the Stokes drift shear goes to infinity as $z^{-1/2}$ and decreases to near zero below depths of about 40 m, so that the strength of the wave–current interaction forcing varies from infinite to near-zero over a relatively shallow mixed layer.

This paper starts with the approximation that the eddy viscosity and diffusivity associated with background turbulence are constant throughout the mixed layer. There are obvious shortcomings to this approach. Although in reality Langmuir cells and the background diffusion occupy different parts of the turbulence spectrum, it is difficult to state exactly where the separation between the large-scale and small-scale turbulence should be made. Additionally, it can be deceptive to treat the small-scale and large-scale turbulence as independent of each other, as will be discussed later in this paper. However, despite these limitations, one can still derive much useful insight from treating the turbulence as constant and focusing on how the vertical variation of Stokes drift and Eulerian shears affect the structure and development of Langmuir cells. The basic questions are: (i) Given a forcing mechanism whose strength is a function of depth, how does one define a 'typical' value for the forcing rate given cells that penetrate to a particular depth? (ii) Does the forcing rate fall off more quickly than the diffusion rate (so that the background diffusion can limit the depth of penetration) or is the reverse true? (iii) How do the typical forcing and diffusion rates determine the typical rate for overturning associated with finite-amplitude cells? (iv) Can Langmuir cells penetrate into stable stratification? How far into the stratification do they penetrate?

Although this paper concentrates on a specific application to Langmuir circulation, with constant background diffusion, the general questions raised above can be applied to a number of problems of more general geophysical interest. Particular examples include convection with non-constant background diffusion (frequently found in atmospheric boundary layers), stellar and planetary-scale convection driven by an

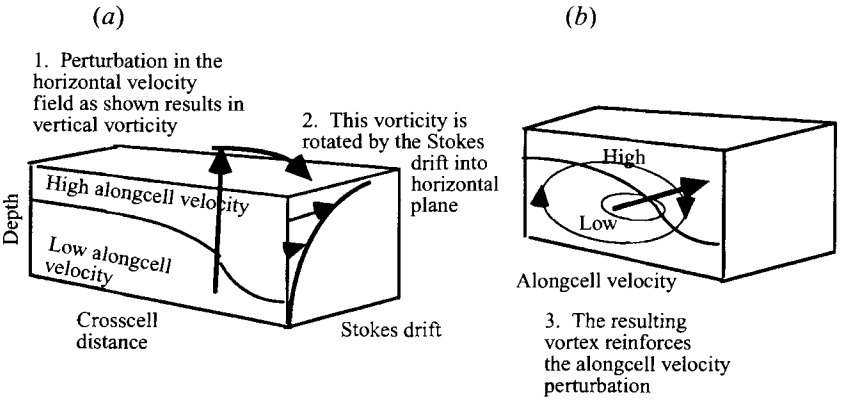

FIGURE 1. Schematic of the wave–current interaction mechanism of Craik & Leibovich (1976) assumed herein to drive Langmuir circulation.

internal heat source where the strength of gravity changes with distance from the centre of the body, and convection in cold freshwater lakes (where the temperature is $< 4°$ C) driven by the deposition of solar radiation.

The problem of how to define the characteristic rates and link them to the forcing is treated as follows. The background turbulence is assumed to set up an equilibrium velocity and density profile within a layer of depth D. Then Langmuir cells then grow upon this profile, altering the shear and stratification and replacing small-scale turbulence as the dominant transport mechanism over some portion of the layer. The initial profile, however, is important in that it still determines the characteristic rates. This approach is different from that of previous workers who either supposed that the water column was initially at rest (Leibovich 1977*a*; Leibovich & Paolucci 1981), that the Stokes drift shear was constant with depth (Cox & Leibovich 1993), or who neglected the effects of viscosity (Leibovich 1977*b*). An additional difference between this and previous work is that the eddy Prandtl number is taken as 1. This is a more realistic assumption for turbulent boundary layers than taking the eddy Prandtl number as equal to the molecular Prandtl number (Leibovich & Paolucci 1981). The advantage of this approach is that it enables analysis of how the presence of cells should alter the equilibrium mixed layer.

The structure of this paper is as follows. In §2 the equations of motion are introduced and methods of solving them using the energy balance equations are discussed. Section 3 considers the physics involved in setting the characteristic scales for forcing in linearly unstable cells. Section 4 extends this theory to finite-amplitude Langmuir cells and presents some result from finite-difference code runs linking the characteristic scales calculated from the background flow to the motions associated with finite-amplitude cells. Section 5 considers some implications of these results for mixed layers in oceans and lakes. Section 6 concludes this paper.

2. Equations of motion and methods of solution

2.1. *The equations*

The scenario considered in this paper is shown in figure 2. The Langmuir cell axis is assumed to be aligned with the wind and waves, pointing in the $+x$-direction. The crosscell direction is the $+y$-direction and the z-axis points upwards. The cells are

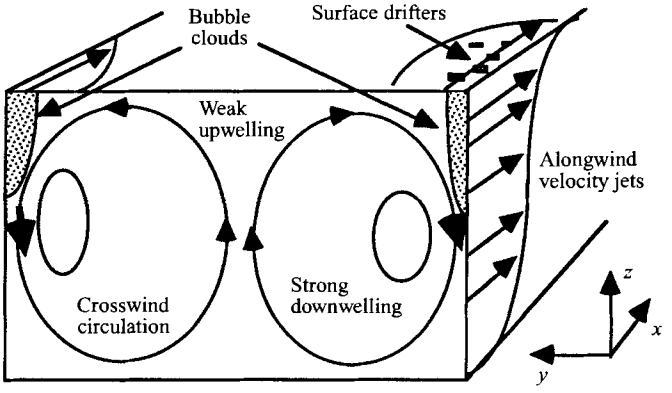

FIGURE 2. Schematic of Langmuir Circulation as studied in this paper. For purposes of this paper, cells are assumed to lie parallel with the wind ($+x$-direction). The cross-cell direction is the y direction and up is the $+z$-direction.

assumed to be invariant in the x-direction. They are embedded within a layer of depth D, in which the mixing coefficients for density and velocity are taken to be constant.

The equations of motion are taken from Gnanadesikan (1994). They consist of transport equations for alongcell vorticity, alongcell velocity, and density:

$$\frac{\partial \Omega}{\partial t}+v\frac{\partial \Omega}{\partial y}+w\frac{\partial \Omega}{\partial z}=-\frac{\partial u_s}{\partial z}\frac{\partial u}{\partial y}-Ri\frac{\partial \rho}{\partial y}+La\nabla^2\Omega, \tag{1a}$$

$$\frac{\partial u}{\partial t}+v\frac{\partial u}{\partial y}+w\frac{\partial v}{\partial z}=-\frac{\partial p}{\partial x}+La\nabla^2 u, \tag{1b}$$

$$\frac{\partial \rho}{\partial t}+v\frac{\partial \rho}{\partial y}+w\frac{\partial \rho}{\partial z}=La\nabla^2\rho, \tag{1c}$$

$$\Omega=\nabla^2\psi, \quad \frac{\partial \psi}{\partial y}=w, \quad \frac{\partial \psi}{\partial z}=-v, \tag{1d,e}$$

$$La=\frac{\nu_e}{a_w^2\sigma}, \quad Ri=\frac{N^2}{k_w^4 a_w^4 \sigma^2}, \tag{1f}$$

$$k_w^{-1}(x,y,z)=(x,y,z), \tag{1g}$$

$$(k_w a)^2\frac{\sigma}{k_w}(u,u_s,u_*,w)=(u,u_s,u_*,v,w), \quad \frac{1}{k_w^2 a_w^2 \sigma}t=t, \tag{1h,i}$$

$$k_w^2 a_w^4 \sigma^2 p=\frac{p}{\rho_0}, \quad u_*^2=\frac{\tau}{\rho_0}. \tag{1j}$$

In these equations k_w, a_w, and σ are the wavenumber, amplitude and frequency of the driving waves, ν_e is the eddy viscosity, N is the buoyancy frequency, u_s is the Stokes drift, t is the surface stress, and u_* is the friction velocity. The script quantities are dimensional, with equations (1g–i) giving the conversion to non-dimensional units. Equation (1j) defines the pressure gradient and stress terms. The wave–current interaction mechanism enters through the vortex forcing term $(\partial u/\partial y)(\partial u_s/\partial z)$ in equation (1a). This term represents the tipping of the relative vorticity associated with the current jets $(\partial u/\partial y)$ by the Stokes drift associated with the surface gravity waves

described in figure 1. These equations are quite similar to those presented by Leibovich (1977*a*). The main differences are a slightly different scaling for the alongcell velocity and that the diffusion coefficients for density and velocity are equal. The key non-dimensional numbers are the Langmuir number La and the Richardson number Ri which are measures of the strength of diffusion and stratification respectively.† At the upper surface ($z = 0$) the stress is set by the wind stress, while at the bottom of the layer ($z = -D$) the shears and thus the viscous stress are set equal to zero:

$$La\left.\frac{\partial u}{\partial z}\right|_{z=0} = u_*^2, \quad \left.\frac{\partial v}{\partial z}\right|_{z=-D} = \Omega|_{z=0} = \Omega|_{z=-D} = 0. \tag{2a, b}$$

The latter condition has been shown to be a useful approximation by Weller (1981) who demonstrated that except at near-inertial frequencies, the effect of the wind stress does not penetrate deeply into the main thermocline.

In the absence of Langmuir cells, the equilibrium velocity profile is given by

$$U(z) = u_*^2\frac{(z+D)^2}{2D} + \left(\frac{u_*^2}{D} - \frac{\partial p}{\partial x}\right)t + C, \tag{3}$$

where C is an undetermined constant which can be set equal to zero without altering the fundamental dynamics. In order to obtain a constant solution, the pressure gradient which is required to balance the wind stress is $\partial p/\partial x = u_*^2/D$ (note that all quantities are non-dimensional).

The boundary conditions on density are chosen so as to allow the water below the layer of strong mixing to serve as a reservoir of dense water, while accounting for a density flux through the upper surface

$$\rho = D, \quad z = -D, \tag{4a}$$

$$\frac{\partial \rho}{\mathrm{d}z} = -1, \quad z = 0. \tag{4b}$$

Note again that the quantities are non-dimensional. In dimensional terms, (4*a*) will read $\rho = \rho_0 N_0^2 D/g$.

The wave field is specified in terms of the Stokes drift. Two Stokes drift profiles are used to force the cells, one corresponding to a monochromatic wave train, the other corresponding to a Pierson–Moskowitz spectrum:

$$u_s(z) = \exp(2z) \quad \text{(monochromatic waves)}, \tag{5a}$$

$$u_s(z) = \int_{f=0}^{\infty} \frac{5}{f^2}\exp\left(-1.25\frac{1}{f^4}\right)\exp(2f^2 z)\,\mathrm{d}f \quad \text{(P–M spectrum)}, \tag{5b}$$

where f is a dummy variable denoting the wave frequency. For the Pierson–Moskowitz spectrum, k_w and σ are taken from the wavenumber and frequency at the spectral peak and the wave amplitude a_w is the total r.m.s. amplitude.

The scenario defined by the above equations is not accurate for deep open-ocean mixed layers, where the Coriolis force rather than a pressure gradient balances the surface momentum input. When this is the case, the Eulerian shear is not parallel with the Stokes drift, and so the cells do not line up with the wind exactly. The effects of Coriolis forces on the instability are considered in Gnanadesikan (1994) and

† The definition of La proposed here differs from that of Leibovich (1977*a*), but conforms to that of Huang (1979) and Gnanadesikan (1994). It allows for a clearer separation between the effects of changing the wind stress, Stokes drift, and the background eddy viscosity.

Gnanadesikan & Weller (1995). Additionally, the steady-state case for (1*c*) with boundary conditions (4*a*, *b*) is one in which the density flux is constant throughout the layer, something which is only approximately true on long (seasonal) timescales rather than on the much shorter ones associated with Langmuir cells.

An additional weakness of the idealization used in this paper is that the mixing coefficient, *La*, is assumed to be constant throughout the mixed layer. This is unlikely to be the case. When comparisons are made between the results presented here and real oceanic mixed layers, the Langmuir number should be thought of as setting the overall level of mixing, not the exact value at any given depth. It should be noted however, that a constant eddy viscosity is predicted by Mellor–Yamada-type models which have been applied to the ocean (Klein & Coste 1984) in which a constant turbulent lengthscale is assumed. In such models, the turbulent diffusion generally scales as the friction velocity multiplied by some fraction of the mixed layer depth. Such a formulation will be used later in this paper. Previous work on Langmuir cells by a large number of investigators (Leibovich 1977*a*; Leibovich & Paolucci 1981; Leibovich, Lele & Moroz 1989; Cox & Leibovich 1993; Gnanadesikan 1994) has also assumed constant turbulent diffusivity and viscosity. Finally, although the scenario here is idealized, the basic principle of evaluating the degree of instability by defining an averaged Stokes drift shear, Eulerian shear, and stratification is one that can be extended to real cases.

2.2. *Solving the equations for unstable growth*

Leibovich (1977*b*) solved for the instability of the above equations in the absence of viscosity. He showed that given an initial profile of velocity $U(z)$, Stokes drift $u_s(z)$ and buoyancy frequency $N^2(z)$ the maximum growth rate is given by

$$\gamma_{max}^2 = \max\left(\frac{\partial U}{\partial z}\frac{\partial u_s}{\partial z} - N^2\right) = \max\left(\gamma_{CL_L}^2(-N^2)\right), \tag{6}$$

where the maximum is taken over depths. Essentially, γ_{CL_L} (referred to hereafter as the *local Craik–Leibovich instability parameter*) represents the strength of the wave–current interaction mechanism driving the cells. This formulation yields some useful insights into whether or not stratification can shut off Langmuir cells (obviously if $N > \gamma_{CL_L}$ everywhere it can). It is not sufficient to give a good understanding of the importance of wave–current interaction in the field, however, for three main reasons. (i) In the field the strength of the wave–current interaction mechanism needs to be evaluated separately from the background turbulent diffusion driven by such processes as Kelvin–Helmholtz instability which are responsible for setting up the background shear and stratification. (ii) When the waves are represented by a spectrum, γ_{max} as predicted by (6) is very sensitive to the Stokes drift shear right at $z = 0$. This quantity is dominated by high-frequency waves which are not generally measured. For a Pierson–Moskowitz spectrum γ_{max} is infinite, and so (6) yields no information about how stratification affects the cells. (iii) One question of interest is the depth to which the cells mix. It is unclear from (6) alone whether to expect that this depth is that at which $\gamma_{CL_L}^2$ becomes negative, or whether the high shear near the surface can drive penetrative motions into the stratified thermocline below.

As will be shown below, significant understanding can be gained by replacing the local Craik–Leibovich instability parameter with one in which the local Eulerian shear, Stokes drift shear and stratification are replaced by weighted averages over the depth of penetration. The depth-weighted parameterization does a much better job at predicting the mixing depth and the strength of overturning, and also in evaluating whether or not stratification and viscosity are capable of capping off the cells.

The key to understanding the solutions presented in this paper is the use of balance equations for the first and second moments of momentum and density. The energy balance equations may be derived by letting

$$u = u'(x,z,t) + U(z,t), \quad v = v'(x,z,t) + V(z,t), \tag{7a,b}$$

$$w = w'(x,z,t), \quad \rho = \rho'(z,t) + P(z,t). \tag{7c,d}$$

The equations for the variance in crosscell velocity, alongcell velocity, and density are then

$$\frac{\partial}{\partial t}\int_{-D}^{0} \overline{v'^2 + w'^2}\,\mathrm{d}z = -\int_{-D}^{0} \overline{v'w'}\frac{\partial V}{\mathrm{d}z}\mathrm{d}z - \int_{-D}^{0} \overline{u'w'}\frac{\partial u_s}{\partial z}\mathrm{d}z - Ri\int_{-D}^{0} \overline{\rho'w'}\,\mathrm{d}z$$
$$- La\int_{-D}^{0} \overline{\frac{\partial v'^2}{\partial y} + \frac{\partial v'^2}{\partial z} + \frac{\partial w'^2}{\partial y} + \frac{\partial w'^2}{\partial z}}\,\mathrm{d}z, \tag{8a}$$

$$\frac{\partial}{\partial t}\int_{-D}^{0} \overline{u'^2}\,\mathrm{d}z = -\int_{-D}^{0} \overline{u'w'}\frac{\partial U}{\mathrm{d}z}\mathrm{d}z - La\int_{-D}^{0} \overline{\frac{\partial u'^2}{\partial y} + \frac{\partial u'^2}{\partial z}}\,\mathrm{d}z, \tag{8b}$$

$$\frac{\partial}{\partial t}\int_{-D}^{0} \overline{\rho'^2}\,\mathrm{d}z = -\int_{-D}^{0} \overline{\rho'w'}\frac{\partial P}{\mathrm{d}z}\mathrm{d}z - La\int_{-D}^{0} \overline{\frac{\partial \rho'^2}{\partial y} + \frac{\partial \rho'^2}{\partial z}}\,\mathrm{d}z. \tag{8c}$$

The integrals on the right-hand side of (8*a*) represent the shear production, the energy flux generated by the wave spinning up the vortices in the x-direction, the buoyancy flux, and the dissipation respectively. The energy flux introduced by the wave–current interaction is hereafter referred to as the *Stokes production* and represents a transfer of energy from the wave field to the Langmuir cells.

In order to analyse how unstable modes grow in these equations it is necessary to assume that the cells can be approximated by some shape function (denoted by a tilde) multiplied by some amplitude. Then for generality:

$$u' = u_1\tilde{U}(z)\cos(kx)\,\mathrm{e}^{\gamma t}, \quad \rho' = \rho_1\tilde{\rho}(z)\cos(kx)\,\mathrm{e}^{\gamma t}, \quad \psi' = \psi_1\tilde{\psi}(z)\sin(kx)\,\mathrm{e}^{\gamma t}, \tag{9a–c}$$

$$2\int_{-D}^{0} |\tilde{U}(z)|^2\,\mathrm{d}z = 2\int_{-D}^{0} |\tilde{\rho}(z)|^2\,\mathrm{d}z = 2\int_{-D}^{0} |\tilde{\psi}(z)|^2\,\mathrm{d}z = 1. \tag{9d}$$

If the shape functions are expanded in a Fourier series, the resulting series may be truncated and inserted into the momentum equations and a standard Galerkin expansion may be derived (Gottleib & Orzsag 1977). Once this is done, the entire instability problem may be cast as a linear eigenvalue problem. Details of this procedure are given in Gnanadesikan & Weller (1995).

In order to analyse the results of the Galerkin expansion, it is extremely useful to consider the energy balance of the growing cells. This can be done as follows. Let U_0 and P_0 be the initial profiles of alongcell velocity and density respectively and assume that the mean crosscell velocity $V_0(z)$ is zero. Then the crosscell energy equation becomes

$$\frac{\gamma\psi_1^2}{2}\int_{-D}^{0}\left\{\left(\frac{\partial\tilde{\psi}}{\partial z}\right)^2 + k^2\tilde{\psi}^2\right\}\mathrm{d}z = \psi_1 u_1\frac{k}{2}\int_{-D}^{0}\tilde{\psi}(z)\,\tilde{U}(z)\frac{\partial u_s}{\partial z}\mathrm{d}z$$
$$+ Ri\,\psi_1\rho_1\frac{k}{2}\int_{-D}^{0}\tilde{\psi}(z)\,\tilde{\rho}(z)\,\mathrm{d}z - \frac{\psi_1^2 La}{2}\int_{-D}^{0}\left\{\left(\frac{\partial^2\tilde{\psi}}{\partial z^2}\right)^2 + 2k^2\left(\frac{\partial\tilde{\psi}}{\partial z}\right) + k^4\tilde{\psi}^2\right\}\mathrm{d}z. \tag{10}$$

The various components of this equation can be broken down into terms with physical significance. For compactness, the following definitions are made:

$$\hat{U}s_z = \int_{-D}^{0} \tilde{\psi}(z)\,\tilde{U}(z)\frac{\partial u_s}{\partial z}\,\mathrm{d}z, \quad \beta = 2\int_{-D}^{0} \tilde{\psi}(z)\,\tilde{\rho}(z)\,\mathrm{d}z, \tag{11a, b}$$

$$k_\psi^2 = 2\int_{-D}^{0}\left\{\left(\frac{\partial\tilde{\psi}}{\partial z}\right)^2 + k^2\tilde{\psi}^2\right\}\mathrm{d}z, \quad K_\psi^4 = 2\int_{-D}^{0}\left\{\left(\frac{\partial^2\tilde{\psi}}{\partial z^2}\right)^2 + 2k^2\left(\frac{\partial\tilde{\psi}}{\partial z}\right)^2 + k^4\tilde{\psi}^2\right\}\mathrm{d}z. \tag{11c, d}$$

Substituting these terms into (10) and dividing out common terms yields

$$(\gamma + La\,K_\psi^4/k_\psi^2)\,\psi_1 = k\hat{U}s_z/k_\psi^2\,v_1 + Ri\,\beta k/k_\psi^2\,\rho_1. \tag{12}$$

The physical significance of the various terms can now be seen more clearly: $k\hat{U}s_z/k_\psi^2$ gives the rate at which the wave–current interaction takes a velocity perturbation and rotates it so that it becomes a streamfunction perturbation of a given shape. Note that because $w' \sim \partial\psi'/\partial x \sim k\psi_1\,\tilde{\psi}(z)$, the product $\tilde{U}(z)\,\tilde{\psi}(z)$ gives the shape of the nonlinear momentum transport associated with the cells. Thus $\hat{U}s_z$ can be interpreted as a weighted average of the Stokes drift shear, where the weighting function depends on the shape of the vertical eddy momentum transport.

Other terms in equation (12) have physical significance as well. K_ψ is the effective wavenumber for the damping of the vorticity. k_ψ is the effective wavenumber which gives the relationship between the streamfunction and vorticity fields. $La\,K_\psi^4/k_\psi^2$ is thus the rate at which cells with a given shape are damped out by the background turbulence field. $Ri\,\beta k/k_\psi^2$ is the rate at which a density perturbation with shape $\tilde{\rho}(z)\,\mathrm{e}^{\mathrm{i}kx}$ produces a streamfunction perturbation of shape $\tilde{\psi}(z)\,\mathrm{e}^{\mathrm{i}kx}$.

In order to see how these terms combine to produce a growth rate, the other variance equations must be analysed as well. Then if for compactness the following definitions are made:

$$\hat{U}_z = 2\int_{-D}^{0} \tilde{\psi}(z)\,\tilde{U}(z)\frac{\partial U_0}{\partial z}\,\mathrm{d}z, \quad \hat{P}_{0z} = 2\int_{-D}^{0} \tilde{\psi}(z)\,\tilde{\rho}(z)\frac{\partial P_0}{\partial z}\,\mathrm{d}z, \tag{13a, b}$$

$$k_u^2 = 2\int_{-D}^{0}\left\{\left(\frac{\partial\tilde{U}}{\partial z}\right)^2 + k^2\tilde{U}^2\right\}\mathrm{d}z, \quad k_\rho^2 = 2\int_{-D}^{0}\left\{\left(\frac{\partial\tilde{\rho}}{\partial z}\right)^2 + k^2\tilde{\rho}^2\right\}\mathrm{d}z \tag{13c, d}$$

the following equations for alongcell velocity and density may also be obtained:

$$(\gamma + La\,k_u^2)\,u_1 = k\hat{U}_z\,\psi_1, \quad (\gamma + La\,k_\rho^2)\,\rho_1 = k\hat{P}_{0z}\,\psi_1. \tag{14a, b}$$

In a parallel to the equation for the streamfunction, (13a) defines a depth-averaged Eulerian shear; k_u and k_ρ are the characteristic wavenumbers for damping the velocity and density perturbations. The *depth-averaged Craik–Leibovich instability parameter* γ_{CL} and depth-averaged buoyancy frequency $\hat{N}$ may be defined as

$$\gamma_{CL}^2 = \hat{U}_z\,\hat{U}s_z, \quad \hat{N}^2 = Ri\,\beta\hat{P}_{0z}. \tag{15a, b}$$

Substituting into (11) then yields the following, cubic equation for γ:

$$(\gamma + La\,K_\psi^4/k_\psi^2)(\gamma + La\,k_u^2)(\gamma + La\,k_\rho^2) = k^2\gamma_{CL}^2/k_\psi^2(\gamma + La\,k_\rho^2) + k^2\hat{N}^2/k_\psi^2(\gamma + La\,k_u^2). \tag{16}$$

The various terms in equation (16) are controlled by the spatial structure of the Langmuir cells. In order to determine the growth rate of the fastest growing mode given a particular set of (k, La, Ri, D) it is necessary to determine the vertical structure function.

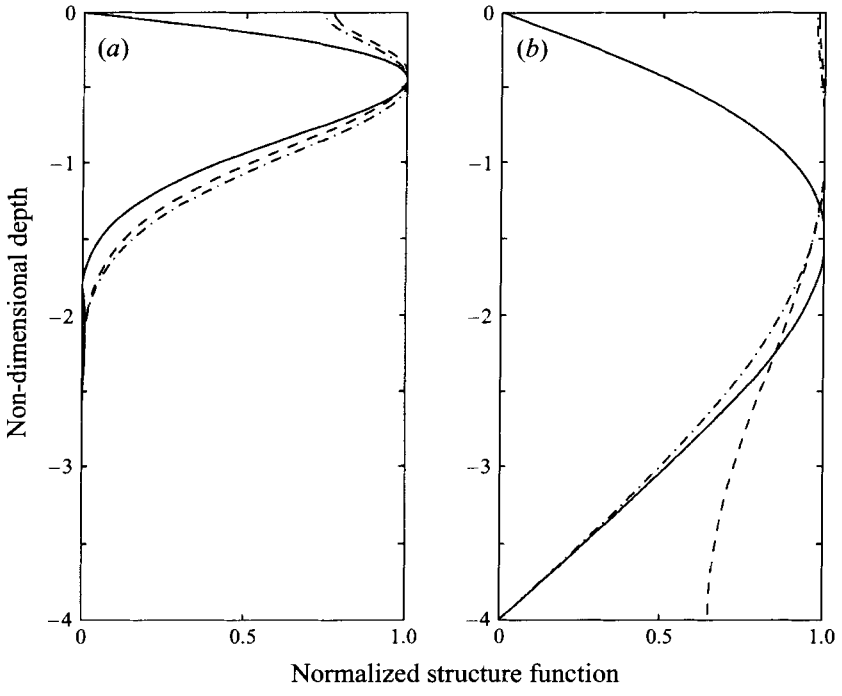

FIGURE 3. Variability in the structure function. Structure functions are calculated using Galerkin code with 40 modes and normalized so that the maximum is 1. The solid line is the streamfunction perturbation, the dashed line the velocity perturbation and the chain–dot line the density perturbation. (*a*) A case where the cells do not feel the bottom, $La = 0.025$, $Ri = 0.25$, $L = 2$. (*b*) A case where the cells do feel the bottom, $La = 0.2$, $Ri = 0.05$, $L = 16$.

As noted above, the shape functions $\tilde{U}(z), \tilde{\rho}(z)$ and $\tilde{\psi}(z)$ can be approximated using a Galerkin approximation. This method is asymptotically valid as the number of terms N in the Fourier series becomes large. All of the results presented here are for $N = 40$, a value for which the growth rates converged. The solutions yielded by the Galerkin code fall into two general classes of interest, illustrated in figure 3. In the first class (figure 3*a*), the cells do not penetrate over the entire domain, and the structure functions for density and velocity perturbations are very similar. This is the case when the stratification is significant or the cell wavelength is much smaller than the layer depth.

When particular analytic forms are assumed for the cell structure, an analytic solution may be found for (16). This is extremely attractive, since it permits simplified analysis of the physics governing the cell structure and growth rate. When considering cases where the cells do not penetrate over the entire domain, the structure functions shown in figure 3(*a*) may be approximated by letting

$$\tilde{\psi} = \frac{1}{D'^{1/2}} \sin(\pi z/D'), \qquad z > -D', \tag{17a}$$

$$\tilde{U}, \tilde{\rho} = \frac{1}{D'^{1/2}} \cos(\pi z/2D'), \qquad z > -D', \tag{17b}$$

$$\tilde{\psi}, \tilde{U}, \tilde{\rho} = 0, \qquad z < -D', \tag{17c}$$

where D' defines the depth over which the cells penetrate. This truncation will be referred to as T1. In the Galerkin code D' will be taken as $2D_{max}$, where D_{max} is the depth at which $|\psi(z)|$ (and hence the vertical velocity) is maximized.

In a second class of cases, shown in figure 3(*b*), the cells penetrate over the entire depth of the layer. For these cases, the velocity perturbation has very little structure with depth. In such cases the velocity and streamfunction perturbations may be approximated as follows:

$$\tilde{\psi} = \frac{1}{D^{1/2}} \sin(\pi z/D), \quad \tilde{U} = 1/(2D)^{1/2}. \tag{18a,b}$$

This truncation, which will be referred to as T2, is of particular interest for long-wavelength cells, cases where the stratification is very weak, or cases when La is large. These truncations are used as tools for understanding the vertical structure both of the linearly unstable and finite-amplitude cells.

2.3. *Solving the equations for nonlinear equilibrium*

As the cells grow, they modify the background velocity profile until a balance is achieved. A schematic of this equilibrium is shown in figure 4. Slow-moving water from the interior is upwelled and accelerated by the wind, creating a velocity jet. The strength of the jet is proportional to the time the water spends at the surface. Suppose there is some equilibrium value at which the torque caused by the waves refracting through the jet balances the viscous deceleration due to the background diffusion. If the cells spin faster than this equilibrium value, the wind will not have time to accelerate the water at the surface, the surface jet will be weaker, and the cells will be spun down by the background turbulence. If the cells are spun more slowly than this equilibrium value, however, the jet will be larger than it is at equilibrium, and the cells will be accelerated by the wave–current interaction mechanism.

The cell amplitude at equilibrium can be analysed (following Malkus & Veronis 1958) using the energy balance equations. At equilibrium, the time-varying terms in the energy balance equations are zero. Additionally, the momentum and density equations may be integrated to yield the following balance equations:

$$-\overline{u'w'} + La\frac{\partial U}{\partial z} = La\frac{\partial U_0}{\partial z}, \quad -\overline{v'w'} + La\frac{\partial V}{\partial z} = 0, \quad -\overline{\rho'w'} + La\frac{\partial P}{\partial z} = La\frac{\partial P_0}{\partial z}. \tag{19a–c}$$

These balance equations may then be used to substitute for the mean shear terms in equation (7). If the following definitions are made:

$$\alpha_v = 2\int_{-D}^{0} (\tilde{\psi}(z)\,\tilde{U}(z))^2\,\mathrm{d}z, \quad \alpha_\rho = 2\int_{-D}^{0} (\tilde{\psi}(z)\,\tilde{\rho}(z))^2\,\mathrm{d}z, \tag{20a, b}$$

then the equations for eddy kinetic energy and density variance become

$$k\tilde{U}s_z v_1 + Ri\beta k\rho_1 = La\,K_\psi^4\psi_1, \tag{21a}$$

$$\psi_1 v_1(k\tilde{U}_z - k^2\alpha_u\psi_1 v_1) = La\,k_u^2 v_1^2, \tag{21b}$$

$$\psi_1\rho_1(k\beta\hat{P}_{0z} - k^2\alpha_\rho\psi_1\rho_1) = La\,k_\rho^2\rho_1^2. \tag{21c}$$

Given a fixed cell structure, these equations can be solved for the amplitude of the streamfunction, velocity, and density perturbation. The method used here (which is described in more detail in Gnanadesikan 1994) is to fix the wavenumber k and choose

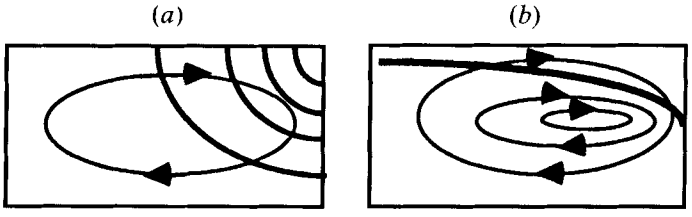

FIGURE 4. Equilibration of Langmuir cells. When cell vortices (shown by thin lines) are much weaker than equilibrium (*a*), a particle brought to the surface and accelerated by the wind spends a long time at the surface. This means that it spends much longer being accelerated by the wind and that the along-cell jet (shown by bold lines) can grow quite strong. In such a case $(\partial u_s/\partial z)(\partial u/\partial y)$ will be very large, and the torque on the cell exerted by the wave–current interaction mechanism will be larger than the diffusive torque $La\Omega/D^2$. When the cell vortex is much stronger than equilibrium (*b*) a particle spends very little time at the surface. In such a case the along-cell jet will be very weak and thus $(\partial u_s/\partial z)(\partial u/\partial y) < La\Omega/D^2$, so the cells will decay diffusively.

a cell structure given some La_c for $\gamma(k, La_c, D) = 0$. (The classical method of picking the wavenumber as well as the structure from the marginally unstable case does not work here, since marginal instability occurs at infinite wavenumber.) The resulting solution is analogous to the first-order weakly nonlinear solution of Malkus & Veronis (1958). This method is used in §4 to consider the modification of the mean structure by the cells. The results are compared to direct integrations of the equations of motion made using a finite-difference code. The details of this code are found in Gnanadesikan (1994). The overall approach follows that of Roache (1977).

3. Physics of linearly unstable Langmuir circulations

3.1. *Unstratified instability: the link between depth of penetration and cell spacing*

The growth rate of unstable Langmuir cells is closely linked to their depth of penetration. This can be seen in figures 5(*a*) and 5(*c*) where $\gamma(k, La, D, u_*)$ and $D_{max}(k, La, D, u_*)$ computed using the Galerkin method are shown as a function of k and La. A consistent pattern emerges in which smaller depths of penetration correspond to larger growth rates. These small penetration depths occur at small wavelengths and small values of Langmuir number. Increasing the Langmuir number decreases the growth rate and increases the depth of penetration. The truncated model T1 introduced in the previous section reproduces this qualitative behaviour (figures 5*b* and 5*d*). Indeed, it captures much of the quantitative behaviour as well. The growth rates are in general underestimated by 10–15% and the depth at which the maximum velocity occurs is overestimated somewhat. The overall pattern here is seen for other layer depths and Stokes drift profiles (Gnanadesikan 1994). One interesting difference is that when the Stokes drift is less strongly peaked at the surface, truncation T1 does an even better job of reproducing the growth rate (as will be demonstrated later in this paper).

Because the wave–current interaction mechanism is strongest near the upper boundary, it is no surprise that the magnitude of the forcing felt by the cells (and hence their growth rate) is a function of the depth over which they penetrate. The question of interest is what governs the depth of penetration. Why, in particular, is the depth of penetration such a strong function of horizontal wavenumber (in contrast to Rayleigh–Bénard convection where the most unstable cells always penetrate over the entire water column)?

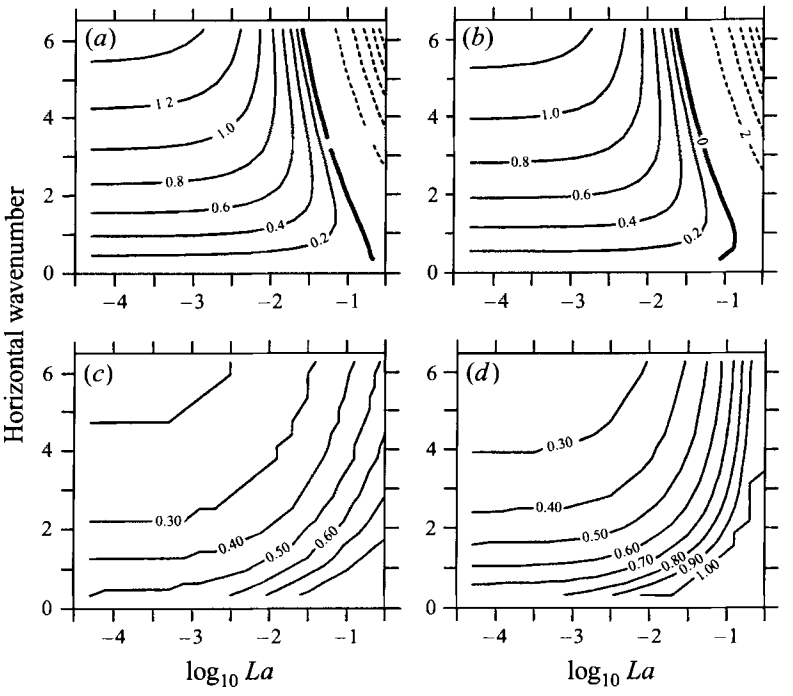

FIGURE 5. Growth rates and depth of maximum vertical velocity $D_{\max}$ of the most unstable mode as a function of non-dimensional horizontal wavenumber (normalized by the wavenumber of the surface gravity waves at the peak of the spectrum) and Langmuir number assuming a Pierson–Moskowitz spectrum, a layer depth of 2 and a surface Eulerian shear of 1. Growth rates are calculated from the full Galerkin code with 40 modes and using truncation T1. (*a*) Growth rate: full Galerkin code. (*b*) Growth rate: truncation T1. (*c*) D_{max}: full Galerkin code. (*d*) D_{max}: truncation T1.

An answer may be found by considering the solution to (16). When density stratification plays no role in the equations, the growth rate is given by

$$\gamma = -\frac{La(k_v^2 + K_\psi^4/k_\psi^2)}{2} + \left[\frac{La^2(k_u^2 + K_\psi^4/k_\psi^2)^2}{4} + \frac{k^2}{k_\psi^2}\gamma_{CL}^2 - La^2\frac{k_u^2 K_\psi^4}{k_\psi^2}\right]^{1/2}. \quad (22)$$

The necessary condition for instability is

$$Ra_{CL} = \frac{k^2\gamma_{CL}^2}{La^2 k_v^2 K_\psi^4} > 0. \quad (23)$$

A better understanding of what the terms in (22) mean may be gained by substituting a truncated representation of the unstable modes. Because the truncated model T1 captures the dependence on Langmuir number and horizontal wavenumber, it is used below to explore the linkage between cell structure and cell penetration. When the shape functions for velocity and density are given by truncation T1 (equation 17*a*, *b*), the growth rate as a function of D' is then

$$\gamma^{T1}(D') = -La(k^2 + (5\pi/8D')^2) + \left[La^2(k^2 + (5\pi/8D')^2) + \frac{k^2}{k^2 + \pi^2/D'^2}(\gamma_{CL1}^2 - \gamma_{diff1}^2)\right]^{1/2}, \quad (24)$$

where

$$\gamma_{CL1}^2 = \frac{4}{D'^2}\int_{-D}^{0} \frac{\partial U_0}{\partial z}\sin(\pi z/D')\cos(\pi z/2D')\,\mathrm{d}z \times \int_{-D}^{0} \frac{\partial u_s}{\partial z}\sin(\pi z/D')\cos(\pi z/2D')\,\mathrm{d}z, \quad (25a)$$

$$\gamma_{diff1} = La(k^2+\pi^2/D'^2)(k^2+\pi^2/4D'^2/k)^{1/2}. \quad (25b)$$

The Craik–Leibovich instability parameter γ_{CL1} gives a measure of the strength of how strongly the cells are driven by wave–current interaction, analogous to the unstable stratification in the Rayleigh–Bénard convection. The characteristic diffusive rate γ_{diff1} indicates the effectiveness of small-scale turbulence at damping the cells. The necessary condition for instability is that the Craik–Leibovich Rayleigh number be supercritical ($Ra_{CL1} = \gamma_{CL1}^2/\gamma_{diff1}^2 > 1$).

The growth rate and structure in the absence of stratification are controlled by a tradeoff between forcing, cell shape, and diffusion. The first part of this tradeoff may be understood by considering the case of inviscid or nearly inviscid instability (as $La \to 0$). In such cases the growth rate of the fastest growing mode as a function of wavenumber is

$$\gamma^{T1}(D') = \frac{1}{(1+\pi^2/k^2D'^2)^{1/2}}\gamma_{CL1}. \quad (26)$$

The growth rate is than a combination of two factors, one that depends only on the cell geometry and one that depends on the Stokes drift and Eulerian shear profiles. The tradeoff between the two may be understood as follows. Let u', v', and w' be characteristic perturbation velocities in the alongcell horizontal, crosscell horizontal and vertical directions respectively. From continuity $kv' + \pi w'/D' = 0$. Then supposing u', v' and w' to all be growing as $\exp(\gamma t)$ the crosscell energy equation yields

$$\frac{\partial}{\partial t}(v'^2+w'^2) \sim \left(\frac{\pi^2}{k^2D^2}+1\right)w'\frac{\partial}{\partial t}w' \sim u'w' \times \text{Stokes drift shear}, \quad (27a)$$

$$\frac{\partial}{\partial t}u'^2 \sim u'\frac{\partial}{\partial t}u' \sim u'w' \times \text{Eulerian shear}. \quad (27b)$$

These equations may be combined as follows:

$$\frac{\partial^2}{\partial t^2}u' = \frac{\partial w'}{\partial t} \times \text{Eulerian shear} \sim u' \times \left(\text{Eulerian shear} \times \text{Stokes drift shear} \times \frac{1}{1+\pi^2/k^2D'^2}\right), \quad (28)$$

so that

$$\gamma \sim \frac{1}{(1+\pi^2/k^2D'^2)^{1/2}}\gamma_{CL}. \quad (29)$$

The significance of the two components of the right-hand side of (29) can be understood by considering (27*a*, *b*). Maximizing γ_{CL} optimizes the rate of energy

release resulting from a given stress $u'w'$. If γ_{CL} is small, the Stokes drift shears and Eulerian shears are small so that for a given $u'w'$ the energy release rate is relatively small. If it is large, a given stress results in rapid release of energy. Maximizing kD' optimizes the *efficiency* of the released energy at increasing the stress. If kD' is small, most of the released energy in the crosscell direction goes into horizontal motions which do not directly reinforce the stress. If kD' is large, most of the released energy in the crosscell direction goes into vertical motions, which directly reinforce $u'w'$.

The competition between maximizing the efficiency and maximizing the forcing leads to the observed relationship between cell penetration and horizontal wavelength. For a Pierson–Moskowitz spectrum, as $D' \to 0$, $\gamma_{CL} \to 1/D'^{-1/4}$. However, the geometric factor goes to zero as D', overwhelming the concentration of forcing so that as $D' \to 0$, $\gamma \to 0$. The growth rate goes to zero more quickly for less strongly surface-intensified profiles, such as that given by a monochromatic wave train. However, given a fixed k, as D' becomes much larger than $1/k$ the efficiency asymptotes to unity while the forcing decreases. This means that for fixed k, as $D' \to \infty$, $\gamma \to 0$. Thus for some intermediate value of D' (of order $1/k$) the inviscid growth rate is maximized. At wavelengths which do not feel the bottom, then, the tradeoff between maximizing the forcing and maximizing its efficiency leads to a depth of penetration with a similar scale to the wavelength.

The presence of diffusion introduces a new tradeoff into the equation. As D' gets very small, the diffusive decay rate, which for small D' goes as La/D'^2, gets very large and can overwhelm the Craik–Leibovich instability parameter in equation (24). Minimizing the diffusive decay scale favours cells with a deeper penetration. The growth rate decreases as La increases for two reasons: greater diffusive damping and a decreased ability to take advantage of the higher shears near the surface.

Although truncation T1 does predict the cell structure at moderate to large k, it does not capture the structure at large La or small k (figure 3*b*). This is because cells which penetrate over the entire domain feel the bottom boundary. Because in the present case both the bottom and upper boundaries are fixed-stress boundaries, the effect of diffusion is to smooth out any vertical structure in the velocity perturbation. In such cases truncation T2 is more representative of the velocity structure than truncation T1. When it is substituted into the energy balance equations, the resulting growth rate is

$$\gamma^{T2} = -La\left(k^2+\frac{\pi^2}{2D^2}\right)+\left[La^2\left(k^2+\frac{\pi^2}{2D^2}\right)^2+\frac{k^2}{k^2+\pi^2/D^2}(\gamma_{CL2}^2-\gamma_{diff2}^2)\right]^{1/2}, \tag{30}$$

where

$$\gamma_{CL2}^2 = \frac{2}{D^2}\int_{-D}^{0}\frac{\partial u_s}{\partial z}\sin(\pi z/D)\,\mathrm{d}z\int_{-D}^{0}\frac{\partial U}{\partial z}\sin(\pi z/D)\,\mathrm{d}z, \tag{31a}$$

$$\gamma_{diff2} = La(k^2+\pi^2/D^2). \tag{31b}$$

The necessary condition for instability is then

$$Ra_{CL2} = \gamma_{CL2}^2/\gamma_{diff2}^2 > 1. \tag{32}$$

As k becomes very small γ_{diff2} decreases. But since γ_{CL2} is constant, Ra_{CL} increases as $k \to 0$. This is in contrast to Ra_{CL1}, which becomes less than 1 as k becomes very small. Marginal instability occurs when $k = 0$.

The fact that the strength of the forcing and damping depend so strongly on the horizontal wavelength $L = 1/k$ means that the Craik–Leibovich Rayleigh number also

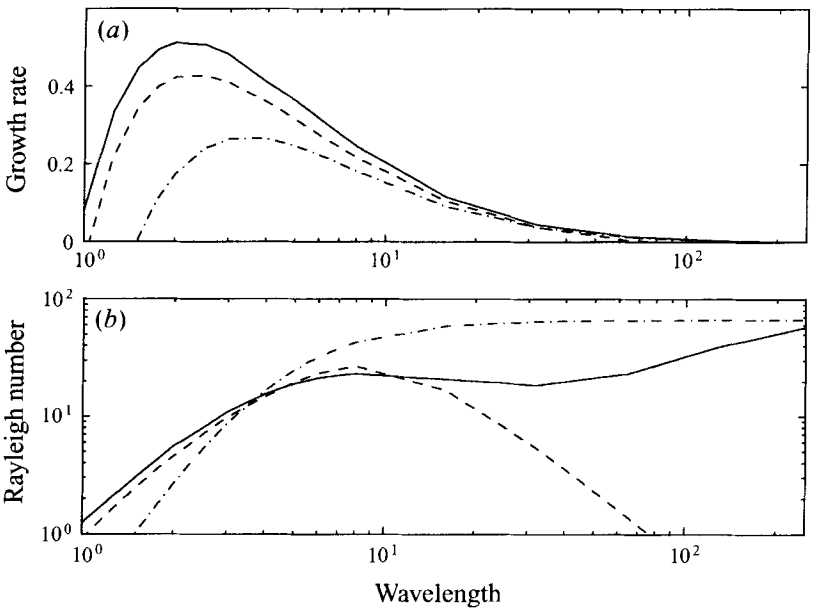

FIGURE 6. The dependence of the growth rate and Craik–Leibovich Rayleigh number on the cross-cell wavelength. All cases assume $La = 0.025$, waves given by a Pierson–Moskowitz spectrum, a layer depth of 2 and a surface Eulerian shear of 1. Solid lines are calculated using the full Galerkin code with 40 modes. Dashed lines are calculated using truncation T1 and chain-dotted lines are calculated using truncation T2. (*a*) Growth rate; (*b*) Craik–Leibovich Rayleigh number.

depends strongly on L. This is illustrated in figure 6. An important point is that Ra_{CL} and γ have different dependence on wavelength. For the particular parameters chosen in figure 6, γ is maximized for cells whose wavelength is roughly the same as the depth of the fluid layer. However, these cells are not very strongly supercritical, with Ra_{CL} being about 5. As the wavelength increases, γ decreases steadily while Ra_{CL} exhibits two maxima, one at wavelengths around 8 (4 times longer than those associated with the fastest growing mode) and another at very long wavelengths. Truncation T1 does a good job in approximating Ra_{CL} for wavelengths smaller than about 12, while T2 captures the behaviour at long wavelength. The different behaviour at different wavelengths reflects the changing structure of the unstable cells. The implications of this fact for cells at equilibrium are considered in §4.

As L, D' become small

$$Ra_{CL} \to D'^{5/2} \to 0 \tag{33}$$

so that the cells become subcritical. This can be seen by the high-wavenumber behaviour in figure 6. Diffusion is stronger than the integrable singularity associated with the Pierson–Moskowitz spectrum and leads to a high-wavenumber cutoff.

The relationship between cell structure and wavelength has important implications for the range of wave frequencies which must be measured in order to accurately characterize the cells. An important point is that the Stokes drift shear right at the surface is not the important shear for driving Langmuir cells. In general, cells which could feel such shears are either extremely inefficient (equation (28)), or damped out by diffusion (equation (33)). Rather, the most important shears are those which contribute to the energy balance of the cells, those at depths where the cells take over the momentum balance. A measure of where the important Stokes drift shears occur as a function of depth of penetration is the depth at which the local Stokes drift shear $\partial u_s/\partial z$

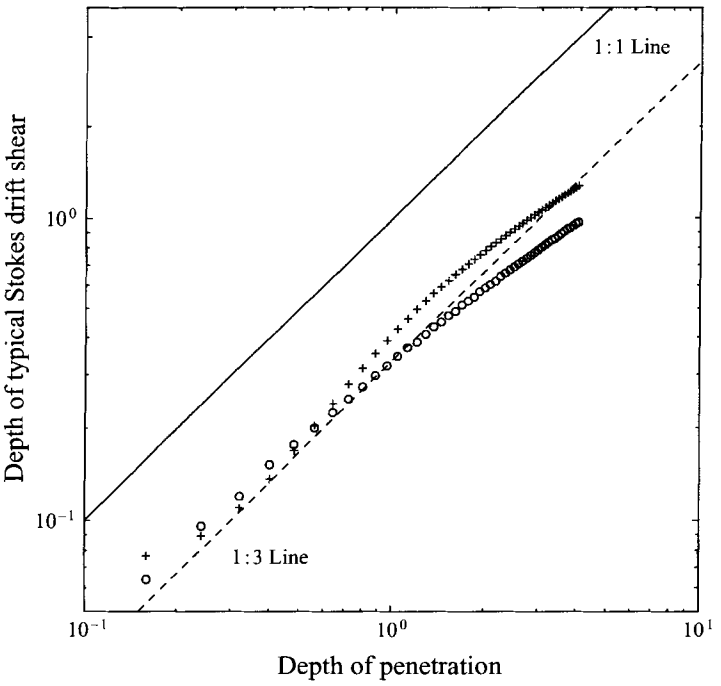

FIGURE 7. Non-dimensional depth at which the depth-averaged Stokes drift shear from truncation T1 equals the local Stokes drift shear. Depths are non-dimensionalized by the inverse wavenumber of the wave at the peak of the spectrum (for 10 s waves 1 unit of depth is about 25 m). +, Monochromatic waves; ○, Pierson–Moskowitz spectrum. Note that the 'typical' shear occurs at about 1/3 the depth of penetration.

is equivalent to the depth-averaged Stokes drift shear $\hat{U}_{sz1}$. Figure 7 shows this depth for two different wave spectra given different penetration depths for the cells. Over most of the range of penetration depths, the 'typical' Stokes drift shear responsible for driving the cells occurs at about 1/3 the cell penetration depth. Since observational oceanographers are primarily interested in cells with penetration scales of at least a few metres, this implies that the important Stokes drift shears are at least 0.5–1 m away from the surface. Waves with frequencies greater than 1 Hz will not contribute significantly to such shears. Thus measurements of wave height up to frequencies of about 1 Hz are sufficient for accurate characterization of Ra_{CL} on scales comparable to the mixed layer.

A question of similar interest to observational oceanographers is whether the cells are capable of penetrating very deep mixed layers. Figure 4 suggests that they are. When $1/k$ and D' become large, assuming exponential decay for the Stokes drift shear,

$$\gamma_{CL} \sim 1/D', \quad Ra_{CL} \sim D'^2. \tag{34a, b}$$

Of course, as D' reaches an upper limit of D and the cells become very long, the Rayleigh number asymptotes to a value close to that given by truncation T2. In very deep mixed layers, however, (34) implies that long-wavelength deeply penetrating cells will be more strongly supercritical even though they may have smaller growth rates. The exponential falloff of the Stokes drift is not strong enough to limit the growth of the cells.

In summary, analysis of the energy balance of linearly unstable unstratified Langmuir cells driven by vertically varying Stokes drift shears reveals the following. (i)

The growth rate and cell structure are closely linked. Cells with long wavelengths grow more slowly than the fastest growing mode, but these longer cells penetrate more deeply into the water column and are more strongly supercritical. (ii) The important Stokes drift shears for driving Eulerian cells occur at some finite fraction of the depth of penetration, not right at the surface. This means that only that portion of the wave spectrum responsible for creating such shears need be measured in the field. If the spectrum has a slope of σ^{-4}, essentially all wavelengths below $1/k$ will contribute equally, whereas for steeper spectral slopes the peak of the spectrum will be more important. (iii) The exponential falloff in the Stokes drift shear is not sufficient to limit deep penetration of the cells in a mathematical sense.

3.2. *Stratified Craik–Leibovich instability: how stratification limits the depth of penetration*

In the examples considered in the preceding sub-section, the depth-averaged forcing was always positive. In the presence of stratification this is not always the case. Stratification opposes the penetration of cells (Lele 1985; Gnanadesikan 1994; Li & Garrett 1995) and can shut off their growth altogether. A sufficient condition for instability to occur in the presence of stratification may be derived by requiring the constant term in (16) be greater than zero. This occurs when the *stratified Craik–Leibovich instability parameter*

$$\gamma_{CLS} = (\gamma_{CL}^2 - \hat{N}^2 k_u^2 / k_\rho^2)^{1/2} \tag{35}$$

is larger than the diffusive decay rate

$$Ra_{CLS} = \frac{\gamma_{CLS}^2}{\gamma_{diff}^2} > 1, \quad \gamma_{diff} = La \frac{k_u K_\psi^2}{k}, \tag{36a, b}$$

where Ra_{CLS} is the stratified Craik–Leibovich Rayleigh number. If the structure functions are given by truncation T1, $k_u^2/k_\rho^2 = 1$ and (16) has a simple analytic solution. The growth rate of the most unstable mode as La becomes small goes to

$$\gamma \sim \frac{k}{(k^2 + \pi^2/D'^2)^{1/2}} \gamma_{CLS1}. \tag{37}$$

Note the parallel between the depth-averaged Craik–Leibovich instability parameter and the local parameter derived by Langmuir (1977*b*) shown in (6). Figure 8 shows the local Craik–Leibovich instability parameter from (6) and the stratified Craik–Leibovich instability parameter from (35) assuming a monochromatic wave train, moderate stratification, and structure functions given by truncation T1. The local instability parameter becomes negative when $D' = 0.6$ while the depth-averaged version only becomes negative when D' is approximately 2.5. Normalized density transports (defined as $\tilde{\psi}(z)\tilde{\rho}(z)$ using the structure functions given by the instability code) are shown for two cases (figure 8*b*). In the case with small wavelength and Langmuir number, the linearly unstable cells transport density only over depths where the local instability parameter is positive. For large La and wavelength, however, the cells penetrate much more deeply and the density transport is large at depths where the local instability parameter is negative. Unstable Langmuir cells are capable of penetrating to depths which are much greater than the local instability parameter would predict. As demonstrated later in this paper, the depth-averaged instability parameter also provides a much better predictor of the depth of penetration of finite-amplitude cells. As will also be shown later, finite-difference code runs which depict the structure of fully developed cells reproduce this behaviour.

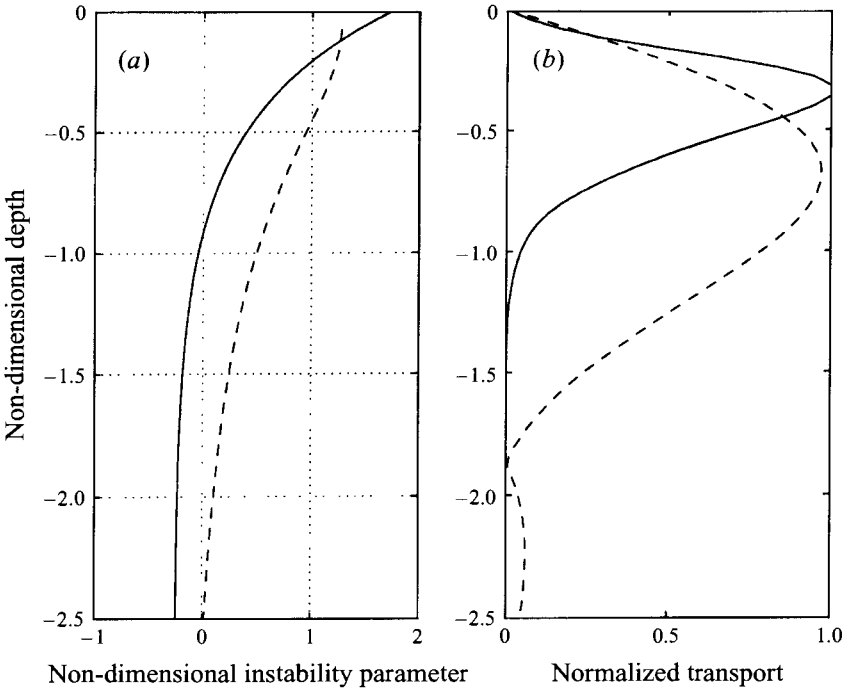

FIGURE 8. Stratified Langmuir cell instability. Case shown assumes monochromatic waves, a surface Eulerian shear of 1, and $Ri = 0.25$. (*a*) Solid line shows the local Craik–Leibovich instability parameter from (7) of Leibovich (1977*b*). Dashed line shows the depth-averaged Craik–Leibovich instability parameter from equation (35). Note that the depth-averaged parameter becomes negative much deeper in the water column. (*b*) Normalized density transport carried by linearly unstable cells for two parameter settings. The solid line is for short-wavelength cells which are not strongly damped ($L = 2$, $La = 0.001$). The dashed line is for long-wavelength cells subject to more diffusion which therefore penetrate much more deeply into the water column ($L = 16$, $La = 0.05$).

The stratified Craik–Leibovich Rayleigh number and growth rate have a dependence on wavelength similar to the unstratified case. Figure 9 shows this dependence for the case in figure 7 given $La = 0.025$. The maximum instability occurs at small wavelengths (1–2), while the Rayleigh number shows two maxima, one at wavelengths of about 8 and the other at very long wavelengths. The truncated model reproduces both the growth rate and the Rayleigh number for a wide range of wavelengths. As in the unstratified case, the boundary conditions at long wavelength can play an important role in determining the structure of the instability. When, as is the case in this study, the destabilizing (velocity) perturbation is less strongly damped than the stabilizing (density) perturbation, the cells can be unstable even though the local instability parameter is negative. The significance of this result for real oceanic cases should not be overemphasized, however, since it occurs for cells which have much longer wavelengths than are commonly seen in the field. The fact that the Rayleigh number asymptotes to the unstratified result is a result of the idealization of the boundary conditions, which do not represent the real ocean. Finally, as will be seen in the following section, the cells with large Ra_{CLS} may take unrealistically long times to develop.

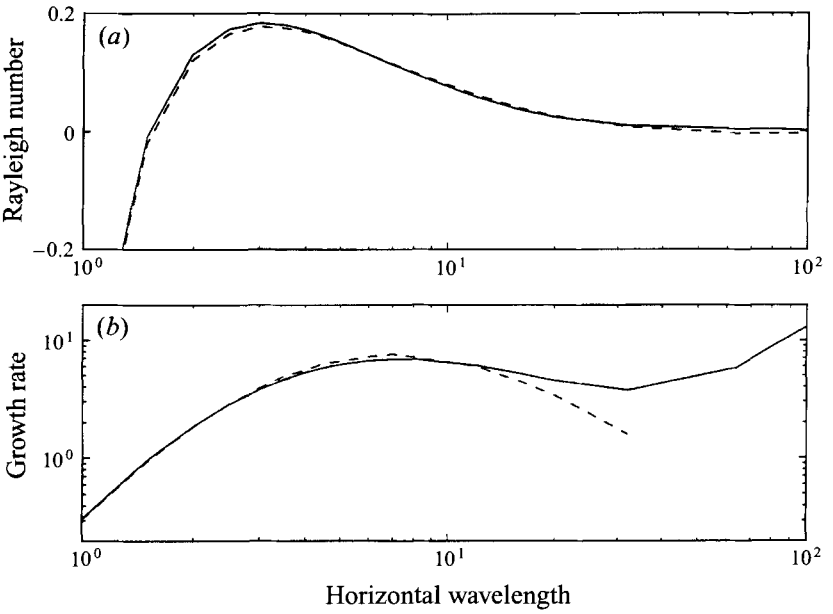

FIGURE 9. The dependence of the growth rate and stratified Craik–Leibovich Rayleigh number on the cross-cell wavelength. All cases assume $La = 0.025$, monochromatic waves, a layer depth of 4 and a surface Eulerian shear of 1. Solid lines are calculated using the Galerkin code with 40 modes. Dashed lines are calculated using truncation T1. (*a*) Growth rate, (*b*) Craik–Leibovich Rayleigh number.

4. Finite-amplitude Langmuir cells

The Craik–Leibovich Rayleigh number based on the cell structure is useful for determining whether cells with such a structure grow. It can also serve as a measure of whether the cells replace small-scale diffusion as the dominant transport mechanism for velocity and density within the mixed layer. This can be seen by considering the solution of equations (21) when the approximation is made that the density and alongcell velocity perturbations have an identical structure. In this case the solution is given by

$$\psi_1 = \frac{1}{K^2\psi}\left[\frac{2}{\alpha_u}(\hat{U}s_z\,\hat{U}_z + Ri\beta^2 P_{0z} - La^2 K_\psi^4 k_u^2/k^2)\right]^{1/2} = \frac{1}{K_\psi^2}\left[\frac{2}{\alpha_u}(\gamma_{CLS}^2 - \gamma_{diff}^2)\right]^{1/2}, \tag{38a}$$

$$\left.\begin{aligned} u_1 &= \frac{La\,K_\psi^2\,\hat{U}_z}{k\gamma_{CLS}^2}\left[\frac{2}{\alpha_u}(\gamma_{CLS}^2 - \gamma_{diff}^2)\right]^{1/2}, \\ \rho_1 &= \frac{La\,K_\psi^2\,\beta P_{0z}}{k\gamma_{CLS}^2}\left[\frac{2}{\alpha_u}(\gamma_{CLS}^2 - \gamma_{diff}^2)\right]^{1/2}. \end{aligned}\right\} \tag{38b, c}$$

The vertical transport of momentum and density accomplished by the cells is then

$$-\overline{u'w'} = \frac{La\,\hat{U}_z}{\alpha_u}(1 - \gamma_{diff}^2/\gamma_{CLS}^2)\,\tilde{\psi}(z)\,\tilde{U}(z), \tag{39a}$$

$$-\overline{\rho'w'} = \frac{La\,\beta P_{0z}}{\alpha_u}(1 - \gamma_{diff}^2/\gamma_{CLS}^2)\,\tilde{\psi}(z)\,\tilde{\rho}(z). \tag{39b}$$

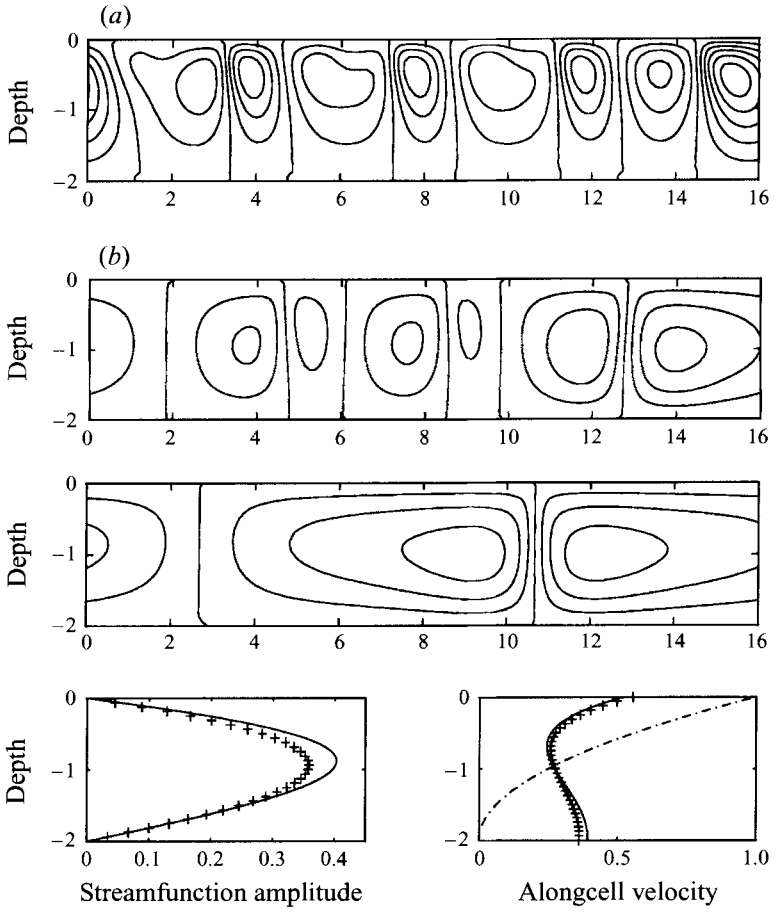

FIGURE 10. Finite-amplitude Langmuir cells. Cases shown here assume (as in figure 4), $La = 0.025$, waves given by a Pierson–Moskowitz spectrum, a layer depth of 2 and a surface Eulerian shear of 1. For 10 s waves with an amplitude of 1 m, 88 time units is 1 day and one length unit is 25 m. For 8 s waves, 240 time units is 1 day, and one length unit is 16 m. (*a*) Perturbation streamfunction, $T = 4$ (contour interval = 0.05). (*b*) Perturbation streamfunction, $T = 40$ (contour interval 0.1). (*c*) Perturbation streamfunction $T = 400$ (contour interval = 0.1). (*d*) Predicted streamfunction amplitude using finite-amplitude theory (solid) and modelled streamfunction (+) at $T = 400$. (*e*) Predicted mean along-cell velocity (solid) from finite-amplitude theory (solid) and model (+) at $T = 400$. Initial condition is shown by chain-dotted line.

Then if $Ra_{CLS} \gg 1$

$$-\overline{u'w'} = \frac{La\,\hat{U}_z}{\alpha_u}\tilde{\psi}(z)\,\tilde{U}(z), \quad -\overline{\rho'w'} = \frac{La\,\beta P_{0z}}{\alpha_u}\tilde{\psi}(z)\,\tilde{\rho}(z). \tag{40a, b}$$

Recalling the definitions of α_v and $\hat{U}_z$ it can be seen that when the Craik–Leibovich Rayleigh number is large, the cells take over that part of the vertical transport of momentum and density which projects on the nonlinear stress profile of the finite-amplitude cells. Insofar as this stress profile has a shape similar to that associated with the linearly unstable cells, Ra_{CLS} is a diagnostic not only of the instability of a water column to cells, but of the ability of the cells to replace small-scale diffusion as the dominant mechanism for vertical transport of both momentum and density.

Because both the depth of penetration and Ra_{CLS} depend on the horizontal

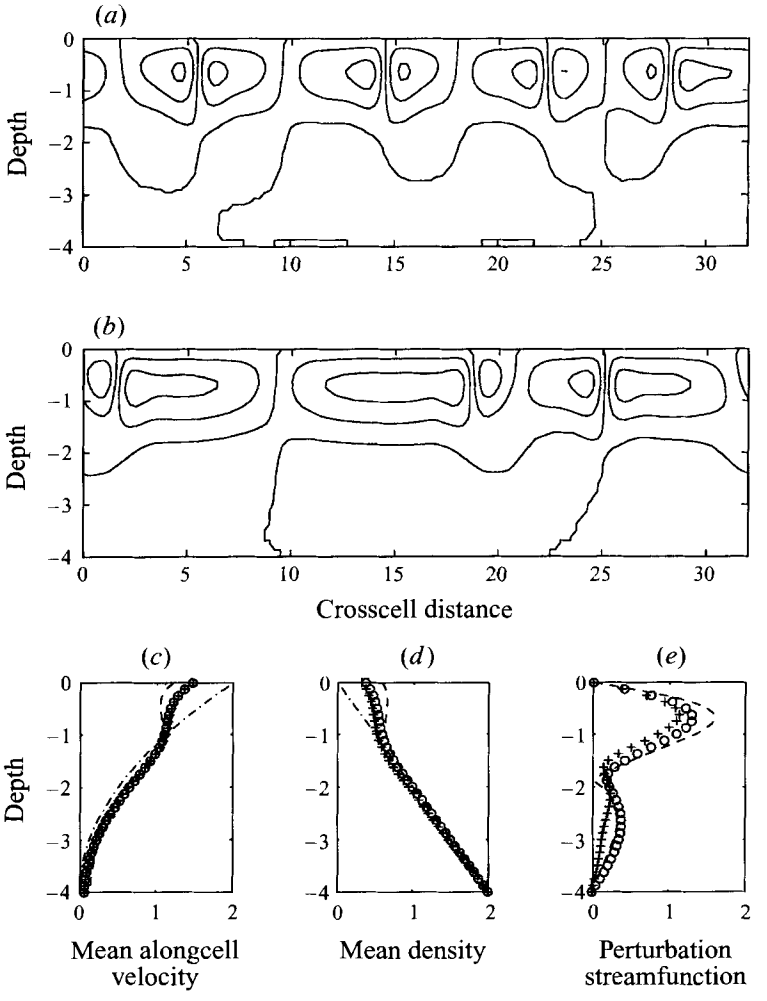

FIGURE 11. Stratified finite-amplitude Langmuir cells. Cases shown here assume (as in figure 9) monochromatic waves. $La = 0.025$, $D = 4$, $Ri = 0.25$, and a surface Eulerian shear of 1. (*a*) Perturbation streamfunction, $T = 160$. (*b*) Perturbation streamfunction, $T = 800$. (*c*) Mean (horizontally averaged) along-cell velocity. Chain–dot line is initial condition; +, model at $T = 160$; ○, model at $T = 800$. The dashed line is the prediction from finite-amplitude theory. (*d*) Same as (*c*) but for mean density. (*e*) Same as (*c*) but for perturbation streamfunction amplitude.

wavenumber, it is extremely important to determine which wavenumbers dominate the solution after finite time. Figure 10 shows the perturbation streamfunction field for the scenario shown in figure 6. Initially, the field is dominated by cells with a spacing which is about twice that of the most unstable mode (these cells have a growth rate, however, only slightly smaller than the most unstable mode). As time evolves, the spacing increases until only one pair of cells is seen in the domain. Similar results were reported by Li & Garrett (1993).

One reason for this evolution in cell size can be understood by considering the different dependence on wavelength of growth rate, depth of penetration and Ra_{CL}. Initially, small-wavelength cells with large growth rates dominate the flowfield. However, because these cells do not penetrate very deeply and have smaller Ra_{CL}, they do not substantially modify the mean velocity profile, which is still unstable to longer-

wavelength cells. Consider the effect of a cell with $Ra_{CL} = 2$ upon the mean velocity profile. From (38*a*) it can be seen that such a cell will remove only 50% of the mean shear which projects upon the shape function $\tilde{U}\tilde{\psi}$. Supposing longer-wavelength cells to have identical shape function $\tilde{U}\tilde{\psi}$ (something which will not be true in general), the effect of the shear on the growth of these cells will be reduced by 50%. By replacing the depth-averaged Eulerian shear $\tilde{U}_z$ by $\tilde{U}_z/2$ in the equations for growth rate, it can be seen that the growth rate of the longer-wavelength cells will be reduced, but only by about 30%. These longer-wavelength cells then dominate the flow field over timescales commensurate with their growth rate. Gnanadesikan (1994) demonstrates that this instability is important for the early stages of cell growth, but that as the cells reach the bottom of the layer it does not explain the transition to longer wavelength.

Once the wavelength of the cells is known, the finite-amplitude theory outlined above successfully reproduces the cell amplitude, and the modification of the velocity profile (figures 10*c* and 10*d*). This is an important result, since it means that the final state in the presence of cells can be deduced, in large part, by linearizing around the final state in the absence of cells.

The physical picture is much the same in the presence of stratification (figure 11). Again the cells evolve to wavelengths which are much longer than the most unstable modes and have much deeper penetration over the water column. These cells replace small-scale diffusion as the dominant mechanism for the vertical transport of momentum and density over their depth of penetration. Note that the 'mixed layer' created by the cells has a depth of about 2, comparable to that predicted by considering the depth-averaged instability parameter in figure 8, but much deeper than that predicted by considering the local instability parameter alone. The concentrated forcing near the surface is able to overcome a certain amount of weak stabilizing stratification to drive deeply penetrating Langmuir cells.

In the real ocean, of course, the Coriolis force plays and important role in setting the mean velocity profile. Despite some difference in the details, the simple non-rotating theory presented here may still yield useful results in some cases where Coriolis forces are present. In particular, Gnanadesikan (1994) and Gnanadesikan & Weller (1995) demonstrate that if the Ekman depth is large compared with the mixed layer depth, the velocity shear upon which the cells grow is essentially identical to that in the absence of Coriolis force and the alongcell momentum balance is very similar. Additionally, if Ra_{CLS} (defined using the alongcell component of velocity and Stokes drift shears) is much larger than 1 the cells are shown to replace small-scale diffusion as the dominant vertical transport mechanism for velocity and density, homogenizing the alongcell velocity profile over the depth of penetration.

5. Implications for mixed layer dynamics

The theory developed here can be used to examine the circumstances under which mixed layers with realistic background levels of turbulence are unstable to Langmuir cells driven by wave–current interaction. The Mellor–Yamada $2\frac{1}{2}$-level turbulence closure model (Mellor & Yamada 1974) with a constant turbulence length was used to generate viscosities in layers given various surface heat flux and wind stress. An initial mixed layer with a depth of 20 m was subjected to forcing for a total of 6 h, after which time the viscosity just below the surface was taken as a representative (though generally high) value for the mixed layer as a whole. For a surface stress of 0.12 Pa, corresponding to a wind speed of approximately 10 m s^{-1}, the model predicts a mean eddy viscosity of 0.02 m^2 s^{-1} over a 20 m deep mixed layer (a reasonable value given

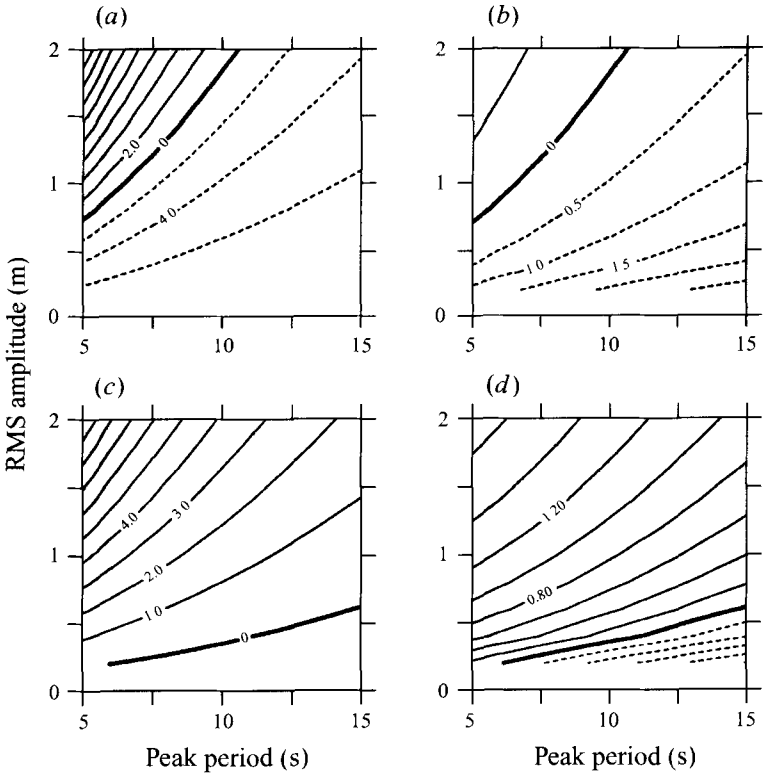

FIGURE 12. Instability to Langmuir cells of a shear flow in a 20 m deep mixed layer. The surface stress is 0.12 Pa (corresponding to a 10 m s^{-1} wind). Eddy viscosity is 0.02 m^2 s^{-1} from a Mellor–Yamada model. There is no heat flux. Waves are given by a Pierson–Moskowitz spectrum. Growth rates and $\log_{10}$ of the Craik–Leibovich Rayleigh numbers are shown as a function of the root-mean-square wave amplitude and the period of the waves at the peak of the spectrum. (*a*) Growth rate ($\times 10^3$) in s^{-1} for cells with 10 m wavelength. (*b*) $\log_{10}(Ra_{CL})$ for cells with 10 m wavelength. (*c*) Growth rate ($\times 10^3$) in s^{-1} for cells with 40 m wavelength. (*d*) $\log_{10}(Ra_{CL})$ for cells with 40 m wavelength.

the results of Weller 1981 and Gnanadesikan 1994). The instability of such a mixed layer to Langmuir cells is shown in figure 12. The degree to which the layer is unstable to Langmuir cells is a strong function of the amplitude and peak period of the surface gravity waves. The profile is strongly unstable when the waves have small periods, but much less strongly unstable for low-period swell. This is because the Stokes drift shear scales as the fifth power of the peak frequency, so that small changes in the frequency can produce large changes in the Stokes drift shear and hence in the degree of instability. As the wave amplitude increases, the cells become more unstable and the Rayleigh number increases. The Rayleigh numbers are larger for long-wavelength (40 m) cells than short-wavelength (10 m) cells, indicating that these longer-wavelength cells would be expected to replace small-scale diffusion as the dominant transport mechanism.

There is a certain danger in treating Langmuir circulations and the background turbulence separately. This can be seen in figure 13, which summarizes instability runs made for a range of heat fluxes, assuming the same wind stress and mixed layer depth as in figure 12 and waves given by a Pierson–Moskowitz spectrum with peak period of 10 s. As before, the eddy viscosities are predicted using a Mellor–Yamada model which does not consider the effect of waves. The dependence on heat flux is rather surprising.

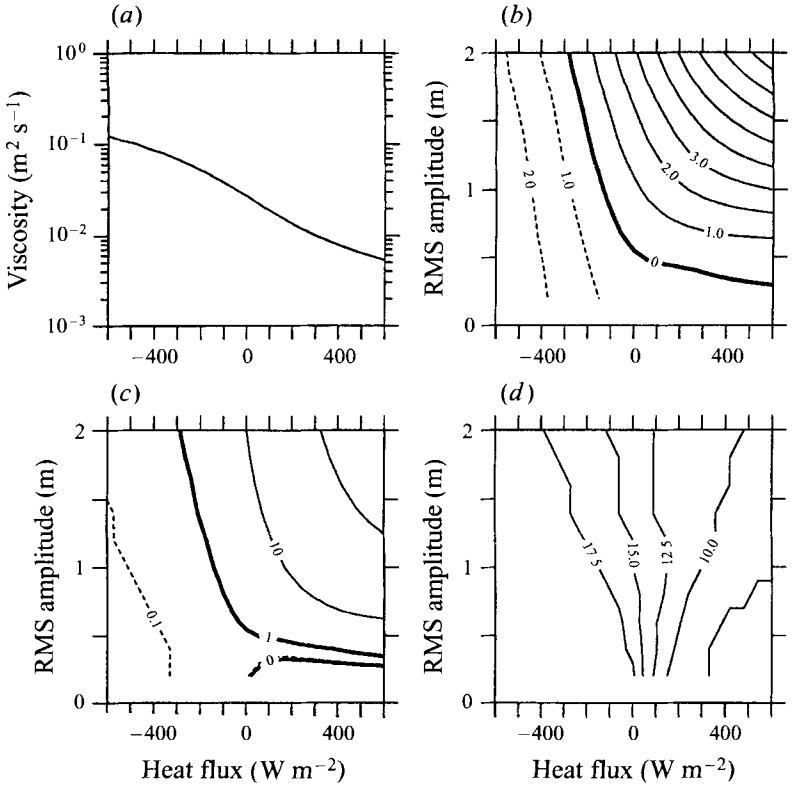

FIGURE 13. Effect of heat flux on Langmuir cell growth. Surface stress is 0.12 Pa, the layer depth is 20 m, and the waves are given by a Pierson–Moskowitz spectrum with a peak period of 10 s. (*a*) Eddy viscosity at 1 m from a Mellor–Yamada model as a function of heat flux. (*b*) Growth rate ($\times 10^3$) in s^{-1} for cells with a wavelength of 40 m. (*c*) Stratified Craik–Leibovich Rayleigh number for cells with a wavelength of 40 m. (*d*) Depth of cell penetration (defined as twice the depth of the maximum vertical velocity) for cells with a wavelength of 40 m.

At low values of wave amplitude, increasing the heat flux stabilizes the water column. However, when the wave amplitude is larger than about 0.5 m (corresponding to a significant wave height of 2 m), increasing the heat flux actually increases the cell strength. As the surface is heated, the turbulence is suppressed, leading to larger and larger surface shears and strong wave–current interaction. For the layer depths shown here, this decrease in the turbulent mixing is more important than the increase in the stratification. The resulting cells are surface-trapped but their depth of penetration increases as the wave height increases (figure 13*d*). The picture which emerges is one in which the Langmuir cell energy is trapped in a narrow surface layer. When the surface is strongly cooled, on the other hand, the increase in turbulent damping is more important than the buoyant forcing on the cells, and the profile predicted by the Mellor–Yamada model becomes stable.

It should be pointed out that the physical scenario in figure 13 is deceptive in terms of predicting Langmuir circulations in the real ocean for the following reasons.

(i) In the real ocean the Coriolis force plays a critical role in reducing instability as the mixing becomes weaker (Gnanadesikan & Weller 1995). As the mixing becomes very weak, interactions between the Stokes drift and the Coriolis force produce and upwind Eulerian shear which reduces the strength of the instability.

(ii) The Mellor–Yamada model implicitly includes the effects of buoyant convection

but not wave–current interaction. As a result, Langmuir cells driven by surface cooling are already included in the Mellor–Yamada model, which will therefore predict overly weak Langmuir cells when the surface cooling is strong. This fact points out the need to consider turbulence and Langmuir cell strength in parallel.

A final interesting implication of the finite-amplitude results is that one can predict the amplitude of the vorticity associated with the cells. Assuming cells given by truncation T1, the vorticity at equilibrium is just

$$\omega = 2(\gamma_{CLS1}^2 - \gamma_{diff1}^2)^{1/2}. \tag{41}$$

Then if Ra_{CLS} is large, the Craik–Leibovich instability parameter γ_{CLS} scales as the frequency of overturning associated with the cells. This has implications for a number of problems.

(i) Creation and penetration of bubble clouds: Langmuir cells have long been suspected to be responsible for the persistent bubble clouds which have been suggested as the principal source of acoustic backscatter (Thorpe 1984*a*, *b*). The depth of penetration of such clouds most probably scales as the depth at which the mixing rate is equal to the consumption rate of the bubbles (Gnanadesikan 1995).

(ii) Velocity structures: the fast mixing times implied by (40) also have implications for the mean Ekman spiral. If $Ra_{CLS} > 1$ the mean Ekman spiral predicted by assuming locally generated isotropic turbulence to drive the mixing will be unstable to Langmuir cells and the cells will homogenize the mixed layer interior. Gnanadesikan & Weller (1995) explore this issue using data obtained during the Mixed Layer Dynamics Experiment.

(iii) Testing the wave–current interaction mechanism in the field: the crosscell shear associated with the cells scales as the vorticity which in turn scales as the Craik–Leibovich instability parameter. Insofar as the spatial scale of the cells is known, the level of the cross-cell shear provides a measure of what processes are responsible for forcing the cells. If Langmuir cells are in fact driven by wave–current interaction, the spatially varying shears will reflect this scaling. Recent work (Gnanadesikan 1994) argues that this relationship does in fact hold for two field experiments.

6. Conclusions

This paper has derived a condition for Langmuir cells driven by wave-current interaction to be capable of replacing small-scale diffusion as the dominant transport mechanism for velocity and density. It has shown that this condition is met under some reasonable circumstances in the absence of Coriolis forces. The rate of mixing caused by finite-amplitude cells is proportional to the depth-averaged forcing, and as such can be quite large. The cells are capable of penetrating to depths much larger than those associated with the forcing mechanism, supporting the contention that they are in fact the dominant mixing mechanism in oceanic mixed layers.

This paper raises a number of issues which will be important in furthering research into Langmuir circulations and their effect on the upper ocean. These include the following.

(i) The nature of the interaction between the cells and the stratified thermocline. The bottom boundary layer used in these runs is highly idealized and differs in its treatment of density and velocity. This plays an important role in setting Ra_{CLS} for long-wavelength cells in a way which may not be a realistic representation of the oceanic thermocline. Cox & Leibovich (1993) considered the effects of a modified boundary condition on the fastest mode over all wavelengths. However, as shown in this paper,

the fastest-growing mode may not feel the bottom, and it may be more realistic to consider the effect on the cells with the largest Craik–Leibovich Rayleigh number.

(ii) The dynamics which govern the equilibrium spatial scales of the cells. The two-dimensional results shown here predict cells which are up to eight times broader than the mixed layer depth. Additionally, the range of cell scales seen in the field is not reproduced by these models. Gnanadesikan (1994) noted that Coriolis forces could interrupt the transfer of energy to larger and larger spatial scales. Thorpe (1992) showed that three-dimensional vortex merging could also play a role in determining the cell structure. The relative importance of these effects is not well understood.

(iii) The effects of vertically variable mixing. The results here approximate the mixing using a constant eddy viscosity. Allowing the eddy viscosity to depend on the local shear (as is done in large-eddy simulations) will allow a better determination of the relative roles of Langmuir cells and small-scale turbulence in stirring the mixed layer.

(iv) The stability of the finite-amplitude solutions. We have not addressed the question here of whether the finite-amplitude solutions are stable. Leibovich *et al.* (1989) showed that under certain conditions, steady Langmuir cells would be replaced by travelling wave solutions. This does not appear to have occurred for any of the cases considered here, and it is unclear whether such effects are due to boundary conditions, or whether it is simply a matter of going to larger values of Craik–Leibovich Rayleigh number.

Thanks are due to Bob Weller, Al Plueddemann, Dave Chapman, Joe Pedlosky, Jim Price, Gene Terray, and Paola Rizzoli for numerous comments on this work. Patrice Klein provided code for the Mellor–Yamada model. Thanks also to Roger Samuelson, Ming Li, and an anonymous referee for comments on earlier drafts. The work reported in this paper is an outgrowth of the author's thesis research, in which he was supported as an ONR Graduate Fellow and a graduate research assistant under the Surface Waves Processes Program N00014-90J-1495. Additional support was provided by ONR under the Acoustic Surface Reverberation Program, grant N00014-91J-1891. Contribution 8951 of the Woods Hole Oceanographic Institution.

REFERENCES

Cox, S. M. & Leibovich, S. 1993 Langmuir circulations in a surface layer bounded by a strong thermocline. *J. Phys. Oceanogr.* **23**, 1330–1345.

Craik, A. D. D. 1970 A wave-interaction model for the generation of windows. *J. Fluid Mech.* **41**, 802–822.

Craik, A. D. D. & Leibovich, S. 1976 A rational model for Langmuir circulation. *J. Fluid Mech.* **73**, 401–426.

Gnanadesikan, A. 1994 Langmuir circulations in oceanic surface layer. PhD Thesis, MIT/WHOI Joint Program in Physical Oceanography; *WHOI Tech. Report* 94–23, 354 pp.

Gnanadesikan, A. 1995 Effects of waves and heat fluxes on bubble patch structure and gas exchange. In *Air–Water Gas Transfer* (ed. B. Jahne & E. A. Monahan) pp. 313–323. Hanau, Germany, AEON Verlag.

Gnanadesikan, A. & Weller, R. A. 1995 The structure and instability of the Ekman spiral in the presence of surface gravity waves. *J. Phys. Oceanogr.* **25**, 3148–3171.

Gottleib, D. & Orszag, S. A. 1977 *Numerical Analysis of Spectral methods: Theory and Applications.* Soc. Ind. Appl. Maths, 170 pp.

Howard, L. N. & Krishnamurti, R. 1986 Large-scale flow in turbulent convection: A mathematical model. *J. Fluid Mech.* **170**, 385–410.

Huang, N. E. 1979 On surface drift currents in the ocean. *J. Fluid Mech.* **91**, 191–208.

KLEIN, P. C. & COSTE, B. 1984 Effects of wind stress variability on nutrient transport into the mixed layer. *Deep-Sea Res.* **31**, 21–37.

LANGMUIR, I. 1938 Surface motion of water induced by wind. *Science* **87**, 119–123.

LEIBOVICH, S. 1977*a* On the evolution of the system of surface wind drift currents and Langmuir circulation in the ocean. Part 1. Theory and averaged current. *J. Fluid Mech.* **79**, 715–743.

LEIBOVICH, S. 1977*b* Convective instability of stably stratified water in the ocean. *J. Fluid Mech.* **82**, 561–583.

LEIBOVICH, S. 1983 The form and dynamics of Langmuir circulation. *Ann. Rev. Fluid Mech.* **15**, 391–427.

LEIBOVICH, S., LELE, S. K. & MOROZ, I. 1989 Nonlinear dynamics in Langmuir circulations and thermosolutal convection. *J. Fluid Mech.* **198**, 471–511.

LEIBOVICH, S. & PAOLUCCI, S. 1981 The instability of the ocean to Langmuir circulations. *J. Fluid Mech.* **102**, 141–168.

LI, M. & GARRETT, C. 1993 Cell merging and the jet/downwelling ratio in Langmuir circulation. *J. Mar. Res.* **51**, 737–769.

LI, M. & GARRETT, C 1995 Is Langmuir circulation driven by surface waves or surface cooling? *J. Phys. Oceanogr.* **35**, 64–76.

MALKUS, W. V. R. & VERONIS, G. 1958 Finite amplitude cellular convection. *J. Fluid Mech.* **4**, 225–260.

MELLOR, G. & YAMADA, T. 1974 A hierarchy of turbulence closure models for planetary boundary layers. *J. Atmos. Sci.* **31**, 1791–1806.

PIERSON, W. J. & MOSKOWITZ, L. 1964 A proposed spectral form for fully developed seas based on the similarity theory of S. A. Kitaigorodskii. *J. Geophys. Res.* **64**, 5181–5190.

ROACHE, P. J. 1977 *Computational Fluid Dynamics.* Hermosa.

SMITH, J., WELLER, R. A. & PINKEL, R. 1987 Velocity structure in the mixed layer during MILDEX. *J. Phys. Oceanogr.* **17**, 425–439.

TERRAY, E. A., DONELAN, M. A., AGARWAL, Y. C., DRENNAN, W. M., KAHMA, K. K., WILLIAMS, A. J., HWANG, P. A. & KITAIGORODSKII, S. A. 1996 Estimates of kinetic energy dissipation under breaking waves. *J. Phys. Oceanogr.* (in press).

THORPE, S. A. 1984*a* The effect of Langmuir circulation on the distribution of submerged bubbles caused by breaking wind waves. *J. Fluid Mech.* **142**, 151–170.

THORPE, S. A. 1984*b* On the determination of K_v in the near-surface ocean from acoustic measurements of bubbles. *J. Phys. Oceanogr.* **14**, 855–863.

THORPE, S. A. 1992 The breakup of Langmuir circulation and the instability of an array of vortices. *J. Phys. Oceanogr.* **16**, 1462–1478.

WELLER, R. A. 1981 Observations of the velocity response to wind forcing in the upper ocean. *J. Geophys. Res.* **86**, 1969–1977.